Graphene Field-Effect Transistor Model With Improved Carrier Mobility Analysis

Jing Tian, Anestis Katsounaros, Darryl Smith, and Yang Hao, *Fellow, IEEE*

***Abstract*— This paper presents a SPICE-like graphene field-effect transistor (GFET) model with an improved carrier mobility analysis. The model considers the mobility difference between the electrons and the holes in graphene, as well as the mobility variation against the carrier density. Closed-form analytical solutions have been derived, and the model has been implemented in Verilog-A language. This was compiled into an advanced design system. The proposed model gives excellent agreement between the simulation results and the measurement data for both the hole and electron conduction simultaneously. The model is suitable for the exploration of GFET-based applications, especially for those using the ambipolar transfer property of GFET.**

***Index Terms*— Field-effect transistor (FET), graphene, mobility, Verilog-A.**

I. Introduction

THE single-atomic-thick nature, high carrier mobility, high thermal conductivity, and ambipolar transfer characteristics make graphene attractive for many electronic applications. Graphene-based ultrabroadband photodetector [1], voltage-tunable terahertz (THz) modulator [2], and broadband millimeter wave absorber [3] have been reported. In [4], the first field-effect transistor (FET) using graphene as the channel material was demonstrated, followed by a 67-nm graphene field-effect transistor (GFET) with an intrinsic cutoff frequency (f_T) as high as 427 GHz in [5]. The high carrier mobility of graphene makes it competitive with the III-V high electron mobility transistors, thus indicating great potential in high-frequency applications.

Over the past few years, GFET-based analog/RF circuits [6], [7], active THz [8], and ionizing radiation detectors [9] have been reported. However, an accurate GFET model to predict the device and circuit performance is still missing. The drift-diffusion GFET model in [10] revealed the physical mechanisms behind the saturation current of the GFETs. However, the accuracy of this model is limited by the accuracy in the calculation of the parameters such as quantum capacitance and saturation velocity. Therefore, a list of work focusing on the theoretical studies [11], [12] and the closed-form analytical solutions [13]–[18] of the GFET modeling were published, providing improved agreement with measurements. A comprehensive model was also reported [19], allowing fast detection of significant physical parameters in the GFET design. Recently, comparisons of existing GFET models were made in [20], leading to a Verilog-A compatible model with the improved accuracy in the vicinity of the Dirac point.

Although these GFET models were in agreement with the measurement data for either electron or hole conduction, modeling of both the conduction modes simultaneously was inaccurate due to the use of identical carrier mobility for both the electrons and the holes. The mobility difference between the electrons and the holes has been observed in many experiments [21]–[23]. This difference can sometimes be as high as 23% [22]. Thus, using the same carrier mobility for the electrons and the holes would cause mismatching for either electron or hole conduction (depending on which mode the model is optimized for). Although there have been reports using distinct mobilities for each of the charge carriers [24]–[26], these models match poorly with the measurement data. Moreover, it has been reported that carrier mobility decreases with the increase in the carrier density in the monolayer graphene [21], [23], but in all the GFET models mentioned above, constant carrier mobility is used.

Therefore, the work presented in this paper aims to create an effective carrier mobility, considering the mobility difference in electron and hole, including the mobility variation against the carrier density. The concept of effective carrier mobility is introduced in Section II. In Section II, based on the comparisons in [20], appropriate approximations for quantum capacitance, charge density, and saturation velocity are chosen. A full derivation of the closed-form analytical solutions of the proposed GFET model is presented in Section III. In Section IV, the modeled results are compared with measurement data. Section V concludes this paper.

II. Aspects of Modeling

The aim of this paper is to derive accurate closed-form analytical solutions for the intrinsic region of GFET (see the schematic in Fig. 1). Thus, in this section, the approximations

Manuscript received June 16, 2015; revised August 6, 2015; accepted August 11, 2015. Date of publication August 31, 2015; date of current version September 18, 2015. This work was supported in part by the Engineering and Physical Sciences Research Council through the Graphene Flexible Electronics and Optoelectronics under Grant EP/K01711X/1 and in part by the European Graphene Flagship under Grant FP7-ICT-604391. The review of this paper was arranged by Editor G. L. Snider. *(Corresponding author: Yang Hao.)*

J. Tian and D. Smith are with the School of Electronic Engineering and Computer Science, Queen Mary University of London, London E1 4NS, U.K. (e-mail: j.tian@qmul.ac.uk; darryl.smith@qmul.ac.uk).

A. Katsounaros and Y. Hao are with the School of Electronic Engineering and Computer Science, Queen Mary University of London, London E1 4NS, U.K. and also with the Cambridge Graphene Centre, Department of Engineering, University of Cambridge, Cambridge CB3 0FA, U.K. (e-mail: ak890@cam.ac.uk; y.hao@qmul.ac.uk).

Color versions of one or more of the figures in this paper are available online at http://ieeexplore.ieee.org.

Digital Object Identifier 10.1109/TED.2015.2469109

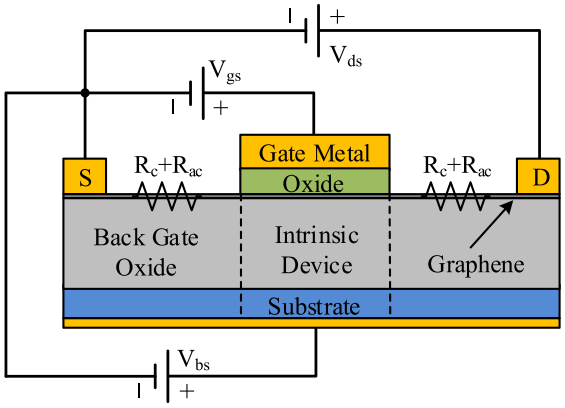

Fig. 1. Cross section of dual-gate GFET modeled in this paper. The channel material is monolayer graphene. V_{gs}: top-gate voltage. V_{bs}: back-gate voltage. V_{ds}: voltage between external drain (D) and source (S) electrodes. Contact and access resistances (R_c and R_{ac}) are considered as one resistance for both source and drain. Intrinsic device is the region covered by the top gate.

chosen for effective carrier mobility, quantum capacitance, charge density, and saturation velocity should match this criteria while retaining reasonable accuracy. The access and contact resistances are modeled as constant resistors on the drain (R_d) and source (R_s) sides.

A. Charge Density in Graphene Channel

The expressions for the electron and hole densities (n and p) in a graphene channel have been derived as [20]

$$n = \frac{2(kT)^2}{\pi(\hbar v_F)^2}\mathfrak{F}_1\left(\frac{-qV_{\rm ch}}{kT}\right) \tag{1}$$

$$p = \frac{2(kT)^2}{\pi(\hbar v_F)^2}\mathfrak{F}_1\left(\frac{qV_{\rm ch}}{kT}\right) \tag{2}$$

where $\mathfrak{F}_1(\cdot)$ is the first-order Fermi–Dirac integral, q is the elementary charge, $\hbar$ gives the reduced Planck constant, v_F is the Fermi velocity in graphene, k is the Boltzmann constant, T is the temperature, and $V_{\rm ch}$ is the channel potential. The total net mobile sheet charge density (assuming hole conduction) can be calculated as $Q_{\rm net} = q \times (p - n)$. $Q_{\rm net}$ is used to derive the expression of quantum capacitance and, sometimes, is also used instead of the charge density relevant for transport $Q_t = q \times (p + n)$ in the calculation of the drain current [11], [14], [15], [18]. According to [20], using Q_t rather than $Q_{\rm net}$ in the electronic transport calculation is one way to improve the accuracy of the GFET models. Since there is no closed-form solution for the first-order Fermi–Dirac integral, (1) and (2) have to be solved numerically to achieve the exact solution of Q_t. In this paper, in order to derive the closed-form analytical solution for the drain current, a simplified expression of Q_t proposed by [17]

$$Q_t = \frac{q\pi(kT)^2}{3(\hbar v_F)^2} + \frac{q^3V_{\rm ch}^2}{\pi(\hbar v_F)^2} \tag{3}$$

is used. The relative error between (3) and the exact Q_t is in the order of 10^{-5}.

In addition to Q_t, another important fraction of channel charge, which should be taken into account, is the residual

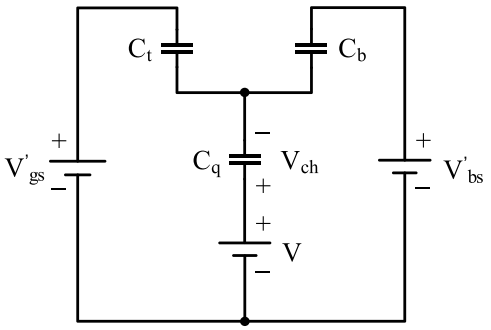

Fig. 2. Equivalent circuit of GFET gate electrostatics describing the relation between gate-oxide capacitances (C_t and C_b) and quantum capacitance C_q. V'_{gs}: net top-gate voltage. V'_{bs}: net back-gate voltage. $V_{\rm ch}$: channel potential. V: voltage drop in the channel.

charge due to electron–hole puddles [21]

$$n_{\rm pud} = \frac{\Delta^2}{\pi(\hbar v_F)^2} \tag{4}$$

where Δ is the inhomogeneity of the electrostatic potential. Thus, the total transport sheet carrier density can be written as

$$Q_{\rm tot} = Q_t + q \times n_{\rm pud} \tag{5}$$

which is used later to calculate the drain current.

B. Quantum Capacitance

Due to the finite density of states of graphene, the effective gate capacitance C_g is smaller than the gate-oxide capacitance $C_{\rm ox}$. A quantum capacitance C_q is, therefore, needed in series with $C_{\rm ox}$ (i.e., $C_g = C_qC_{\rm ox}/(C_q + C_{\rm ox})$; see Fig. 2 to demonstrate the effective gate capacitance in GFET modeling. The value of quantum capacitance is defined as $C_q = -(dQ_{\rm net}/dV_{\rm ch})$ [27]. It is a function of the channel potential $V_{\rm ch}$, which cannot be neglected for a thin gate oxide. The exact expression for C_q has been derived as [27]

$$C_q = \frac{2q^2kT}{\pi(\hbar v_F)^2}\ln\left[2\left(1+\cosh\left(\frac{qV_{\rm ch}}{kT}\right)\right)\right]. \tag{6}$$

C. Effective Carrier Mobility

The carrier mobility describes how fast carriers can move through the graphene channel under certain electric field. Different mobilities for holes and electrons have been measured in graphene [21]–[23]. In [21] and [23], it has also been shown that the carrier mobility decreases with the increase in the carrier density in the monolayer graphene. Therefore, the effective carrier mobility proposed in this paper should not only consider the hole electron mobility difference but also provide a carrier-density-dependent mobility function for the drain current calculations. Assume that the low field mobilities of electrons and holes are μ_n and μ_p, respectively. The effective carrier mobility is defined as

$$\mu_{\rm eff} = \frac{n\cdot\mu_n + p\cdot\mu_p + n_{\rm pud}\cdot h}{n + p + n_{\rm pud}} \tag{7}$$

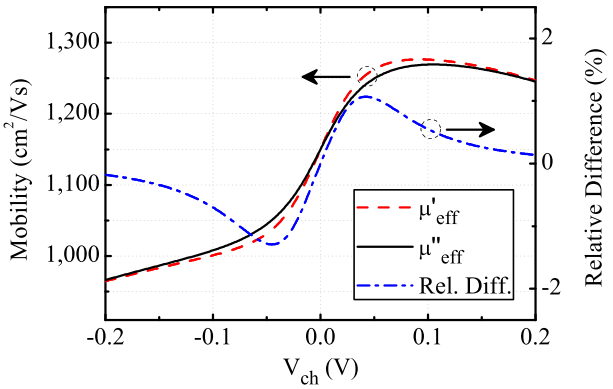

Fig. 3. Left axis: effective carrier mobility as a function of the channel potential V_{ch}—exact model μ'_{eff} and approximation μ''_{eff}. Right axis: relative difference between two models. The parameters used in this graph are $\mu_n = 1000$ cm^2/Vs, $\mu_p = 1300$ cm^2/Vs, $m = 1$ V^2, and $\Delta = 30$ meV.

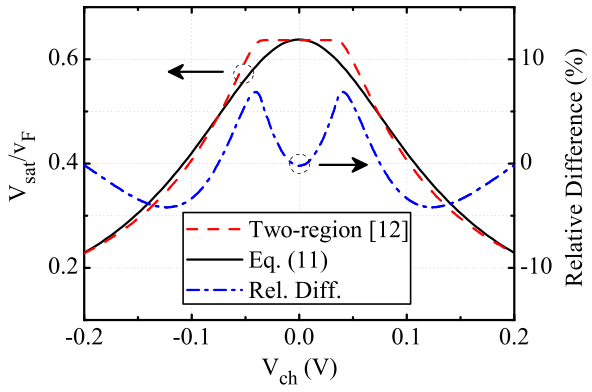

Fig. 4. Left axis: ratio of saturation velocity V_{sat} to Fermi velocity in graphene v_F as a function of the channel potential V_{ch}—two-region model [12] and the proposed approximation. Right axis: relative difference between two models.

where $h = (u_n + u_p)/2$. Thus, the effective carrier mobility is a function of the channel potential V_{ch}. Since the carrier mobility of the monolayer graphene decreases with the increase in the carrier density, an additional term derived from the suggested mobility function in [23] is added to (7)

$$\mu'_{\text{eff}} = \frac{n \cdot \mu_n + p \cdot \mu_p + n_{\text{pud}} \cdot h}{n + p + n_{\text{pud}}} \left(\frac{m}{m + V_{\text{ch}}^2} \right) \tag{8}$$

where m is the square of the reference channel potential, used as an empirical fitting parameter. Equation (8) is rather complicated, and does not result in the closed-form analytical solutions for the drain current. Therefore, an approximate function μ_{pn} for carriers excluding n_{pud} (i.e., for $n + p$ only) is proposed

$$\mu_{pn} = \left(h + \frac{14 z V_{\text{ch}}}{\sqrt{1 + \left(\frac{q V_{\text{ch}}}{(kT \ln(4))} \right)^2}} \right) \left(\frac{m}{m + V_{\text{ch}}^2} \right) \tag{9}$$

where $z = (\mu_p - \mu_n)$. Equation (9) allows calculating the contributions of $n + p$ and n_{pud} to the drain current separately, and enables closed-form solutions for the drain current. Thus, the final effective carrier mobility becomes [using the expression of Q_t from (3)]

$$\begin{aligned} \mu''_{\text{eff}} &= \frac{(n + p) \cdot \mu_{pn} + n_{\text{pud}} \cdot h \cdot \left(\frac{m}{m + V_{\text{ch}}^2} \right)}{n + p + n_{\text{pud}}} \\ &= \left(\frac{14 z (a + b V_{\text{ch}}^2)}{(a + b V_{\text{ch}}^2 + n_{\text{pud}})} \frac{V_{\text{ch}}}{\sqrt{1 + c V_{\text{ch}}^2}} + h \right) \left(\frac{m}{m + V_{\text{ch}}^2} \right) \end{aligned} \tag{10}$$

where $a = \pi (kT)^2/(3(\hbar v_F)^2)$, $b = q^2/(\pi(\hbar v_F)^2)$, and $c = q^2/((kT \ln(4))^2$. In Fig. 3, (8) (red dashed line) and (10) (black solid line) are plotted, as well as the relative difference is defined as $(\mu'_{\text{eff}} - \mu''_{\text{eff}})/\mu'_{\text{eff}} \times 100\%$. It can be seen that μ'_{eff} and μ''_{eff} match very well, and the maximum relative difference is about $\pm 1.5\%$, only in this example.

D. Saturation Velocity

The saturation velocity has been modeled as inversely proportional to the channel potential ($\propto |V_{\text{ch}}^{-1}|$) [14], [16]. This approximation provides accurate V_{sat} at high V_{ch}, but at low V_{ch}, it gives unrealistic results (i.e., infinite V_{sat}). Therefore, a two-region model was proposed in [12], which agrees well with the $\propto |V_{\text{ch}}^{-1}|$ model at high V_{ch}. At low V_{ch}, instead of letting the saturation velocity increase to infinite, the two-region model forces V_{sat} to be a constant value when the charge density Q_{net} is smaller than a predefined factor $\rho_{\text{cri}} = \Omega^2/(2\pi v_F{}^2)$ [12], where Ω is a factor along with $\hbar$ to represent the effective optical phonon emitting energy ($\hbar\Omega$). Thus, the saturation velocity becomes constant around the Dirac point, and this model has also been designed to preserve continuous V_{sat} at ρ_{cri} [12]. The comparison of using $\propto |V_{\text{ch}}^{-1}|$ and the two-region model for saturation velocity (V_{sat}) has also been discussed in [20].

In spite of these benefits, the two-region model has disadvantages. The main problem has been observed is the discontinuity in the calculated transconductance g_m (an important parameter widely used in the analog/RF circuit design), and it becomes even more apparent for higher carrier mobility. This occurs due to the sudden change of saturation velocity function at ρ_{cri}. Although the V_{sat} is designed to be continuous at ρ_{cri}, it does not guarantee the continuity of g_m calculated from $dI_{\text{ds}}/dV_{\text{gs}}$. Meanwhile, the two-region model does not satisfy the requirement of deriving closed-form drain current solutions with (10). Therefore, in this paper, we propose another approximation for V_{sat}

$$V_{\text{sat}} = v_F \left(\frac{e}{1 + f V_{\text{ch}}^2} + g \right) \tag{11}$$

where $e = (V_{\text{sat}}(\max) - V_{\text{sat}}(\min))/v_F$, $f = (q/(5kT))^2$, and $g = V_{\text{sat}}(\min)/v_F$. From the two-region model, the values of $e = 0.58$ and $g = 0.058$ can be extracted. The V_{sat} given by (11) consists of only one function, so that the discontinuities in the calculated g_m are eliminated. In addition, (11) can also be used with (10) to derive the closed-form drain current solutions. Fig. 4 shows the plots

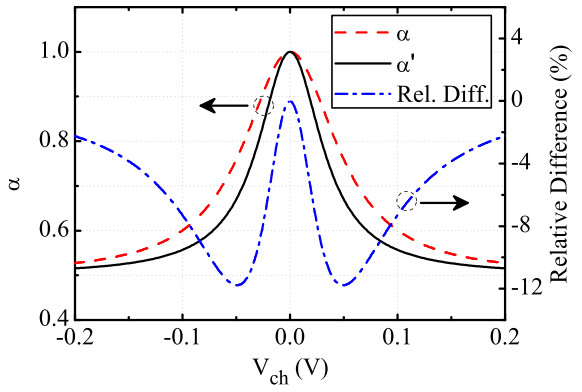

Fig. 5. Left axis: capacitance weighting factor as a function of the channel potential $V_{\rm ch}$—exact model α and approximation α'. Right axis: relative difference between two models.

of (11) and the two-region model. A relative difference $((V_{\rm two-region} - V_{\rm sat})/V_{\rm two-region} \times 100\%)$ within $\pm 7\%$ guarantees the accuracy of the proposed $V_{\rm sat}$ model.

III. Derivation of Proposed GFET Model

This section describes the electrostatics and electronic transport calculation of the proposed GFET model. The drift-diffusion transport model used in this paper is valid when the graphene channel is longer than the mean free path of carriers in graphene. If the channel length is close to or shorter than the mean free path, necessary short-channel effects have to be taken into account.

A. Electrostatics

The equivalent circuit describing the gate electrostatics of the dual-gate GFET is shown in Fig. 2. The expression of channel potential can be derived by applying Kirchhoff's laws to this equivalent circuit as [20]

$$V_{\rm ch} = -\frac{(V_{\rm gs} - V_{\rm gs0} - V)C_t + (V_{\rm bs} - V_{\rm bs0} - V)C_b}{C_t + C_b + \alpha C_q} \tag{12}$$

where $V_{\rm gs}$ and $V_{\rm bs}$ are the top- and back-gate voltages. $V_{\rm gs0}$ and $V_{\rm bs0}$ are the top- and back-gate voltages at which the drain current reaches minimum. V is the voltage drop in the graphene channel. C_t and C_b are the top- and back-gate oxide capacitances, respectively, and α is the capacitance weighting factor defined as [20]

$$\alpha = \frac{Q_{\rm net}}{C_q V_{\rm ch}} = \frac{kT}{qV_{\rm ch}} \frac{\Im_1\left(\frac{qV_{\rm ch}}{kT}\right) - \Im_1\left(\frac{-qV_{\rm ch}}{kT}\right)}{\ln\left[2\left(1+\cosh\left(\frac{qV_{\rm ch}}{kT}\right)\right)\right]}. \tag{13}$$

From the exact model of α [i.e., (13)], one can achieve $\alpha \approx 1$ when $q \times |V_{\rm ch}| \ll kT$ and $\alpha \approx 0.5$ when $q \times |V_{\rm ch}| \gg kT$ [see Fig. 5(red dashed line)]. So far, many existing GFET models use $\alpha = 0.5$ for (12), achieving poor accuracy near the Dirac point [20]. In the case of $\alpha = 1$, an overestimation would be introduced to the calculated drain current away from the Dirac point. Therefore, an accurate model should contain a transition from $\alpha = 1$ at $q \times |V_{\rm ch}| \ll kT$ to $\alpha = 0.5$ at $q \times |V_{\rm ch}| \gg kT$. In this paper, a new model α' providing closed-form analytical solutions to (15) is proposed. It is an approximation of (13) and is given as a function of $V_{\rm ch}$

$$\alpha' = \left(\frac{1}{1 + cV_{\rm ch}^2} + 1\right)\alpha_{\rm min} \tag{14}$$

where $\alpha_{\rm min} = 0.5$ is the minimum value of α. In Fig. 5, a comparison of α and α' is shown. A maximum relative difference $((\alpha - \alpha')/\alpha \times 100\%)$ of -12% is achieved, which guarantees the accurate transition between $\alpha = 0.5$ and $\alpha = 1$ near the Dirac point and is a big improvement compared with the models using constant α.

Finally, to achieve $V_{\rm ch}$ and C_q, (6) and (12) should be solved self-consistently. The iterative Verilog-A algorithm, initially used in carbon nanotube FET models [28], has been extended by Landauer *et al.* [20] to solve self-consistent equations in GFET model successfully. With the iterative Verilog-A algorithm, one is able to let the simulator calculate $V_{\rm ch}$ automatically, greatly simplifying the GFET modeling. Therefore, in this paper, we follow the way of using the iterative Verilog-A algorithm in [20] to calculate the channel potential at the source and the drain (i.e., $V_{\rm cs}$ and $V_{\rm cd}$). During this process, the elementary mathematical approximation of the first-order Fermi–Dirac integral presented in [29] and [30] with a maximum relative error of 1.79×10^{-6} [20] is used.

B. Drain Current Calculation

The drift-diffusion model derived in [11]

$$I_{\rm ds} = \frac{W\int_0^{V_{\rm ds}} \mu Q_{\rm tot} dV}{L + \left|\int_0^{V_{\rm ds}} \frac{\mu}{V_{\rm sat}} dV\right|} \tag{15}$$

is used along with the modeling aspects introduced in Section II to calculate the drain current. To derive the closed-form solution for $I_{\rm ds}$, an accurate square-root-based approximation proposed by [17]

$$C_q = \frac{2q^2 kT\ln(4)}{\pi(\hbar v_F)^2}\sqrt{1 + \left(\frac{qV_{\rm ch}}{kT\ln(4)}\right)^2} \tag{16}$$

is used in this paper. The comparison between (6) and (16) has been discussed in detail by [20].

Deriving the closed-form analytical solution for the integrals in (15) requires replacing dV with $(dV/dV_{\rm ch})dV_{\rm ch}$. In [20], it is derived from (12) as (using $\alpha = 1$)

$$\frac{dV}{dV_{\rm ch}} = 1 + \frac{C_q}{C_t + C_b} \tag{17}$$

neglecting the fact that C_q and α are also the functions of $V_{\rm ch}$. The more accurate expression of $(dV/dV_{\rm ch})$ (for $\alpha = 1$) using the square-root approximation of C_q can be derived as

$$\frac{dV}{dV_{\rm ch}} = 1 + d\sqrt{cV_{\rm ch}^2 + 1} + \frac{cdV_{\rm ch}^2}{\sqrt{cV_{\rm ch}^2 + 1}} \tag{18}$$

where $d = 2q^2 kT\ln(4)/((C_t + C_b)\pi(\hbar v_f)^2)$. Using (17) instead of (18) would cause underestimation to the calculated drain current. In [20], this underestimation is compensated by the overestimation caused using $\alpha = 1$, resulting in an inaccurate estimation of the drain current.

In this paper, the following expression of (dV/dV_{ch}) is derived by substituting (16) and (14) into (12), taking the partial derivative of V against V_{ch} on both the sides of the equation. When simplified yields

$$\frac{dV}{dV_{ch}} = 1 + \frac{ds\left(2 + cV_{ch}^2\left(3 + 2cV_{ch}^2\right)\right)}{\left(1 + cV_{ch}^2\right)^{\frac{3}{2}}}. \tag{19}$$

Finally, by substituting (3)–(5), (9), and (19) into (15) and assuming the effective channel potential to be $(V_{cs} + V_{cd})/2$ for n_{pud}, the numerator integral of (15) can be rewritten as

$$\begin{aligned}\int_{V_{cs}}^{V_{cd}} & q\left(a + bV_{ch}^2\right)\left(h + \frac{14zV_{ch}}{\sqrt{1 + cV_{ch}^2}}\right)\left(\frac{m}{m + V_{ch}^2}\right) \\ & \times \left(1 + \frac{d\alpha_{min}\left(2 + cV_{ch}^2\left(3 + 2cV_{ch}^2\right)\right)}{\left(1 + cV_{ch}^2\right)^{\frac{3}{2}}}\right) dV_{ch} \\ & + \int_0^{V_{ds}} qn_{pud}h\left(\frac{m}{m + \left(\frac{V_{cs}+V_{cd}}{2}\right)^2}\right) dV. \end{aligned} \tag{20}$$

The first term of (20) represents the contribution of Q_t to the drain current, and the second term represents the contribution of qn_{pud} to the drain current. The explicit expression of (20) is achieved with the symbolic calculator in Wolfram Mathematica [31].

Similarly, by substituting (10), (11), and (19) into (15), the denominator integral of (15) can be rewritten as

$$\begin{aligned}\int_{V_{cs}}^{V_{cd}} & \frac{1}{\upsilon_F}\left(\frac{1 + fV_{ch}^2}{e + \left(1 + fV_{ch}^2\right)g}\right)\left(\frac{m}{m + V_{ch}^2}\right) \\ & \times \left(h + \frac{14z\left(a + bV_{ch}^2\right)}{a + bV_{ch}^2 + n_{pud}}\frac{V_{ch}}{\sqrt{1 + cV_{ch}^2}}\right. \\ & \quad + \frac{hd\alpha_{min}\left(2 + cV_{ch}^2\left(3 + 2cV_{ch}^2\right)\right)}{\left(1 + cV_{ch}^2\right)^{\frac{3}{2}}} \\ & \quad \left. + \frac{d\alpha_{min}\left(2 + cV_{ch}^2\left(3 + 2cV_{ch}^2\right)\right)}{\left(1 + cV_{ch}^2\right)^2}\frac{14zV_{ch}\left(a + bV_{ch}^2\right)}{a + bV_{ch}^2 + n_{pud}}\right) dV_{ch}. \end{aligned} \tag{21}$$

The explicit expression of (21) is calculated with the same symbolic calculator used above.

IV. Model Validation

In order to verify the GFET drain current model presented in this paper, the model has been implemented in Verilog-A language and imported in an advanced design system [32]. In this section, the model is first validated against the exact numerical solution results, and the simulated transconductance (g_m) is also compared with the model using two-region saturation velocity [20]. Then, the accuracy of the proposed model near the Dirac point is validated by comparing the modeled results with measurement data from a 2.8-μm gate-length GFET [33]. Finally, the sound behavior of the model is compared with a 20-μm × 15-μm ($L \times W$) GFET measured inhouse as well as two other GFETs from [34] and [35] under conventional biasing regions.

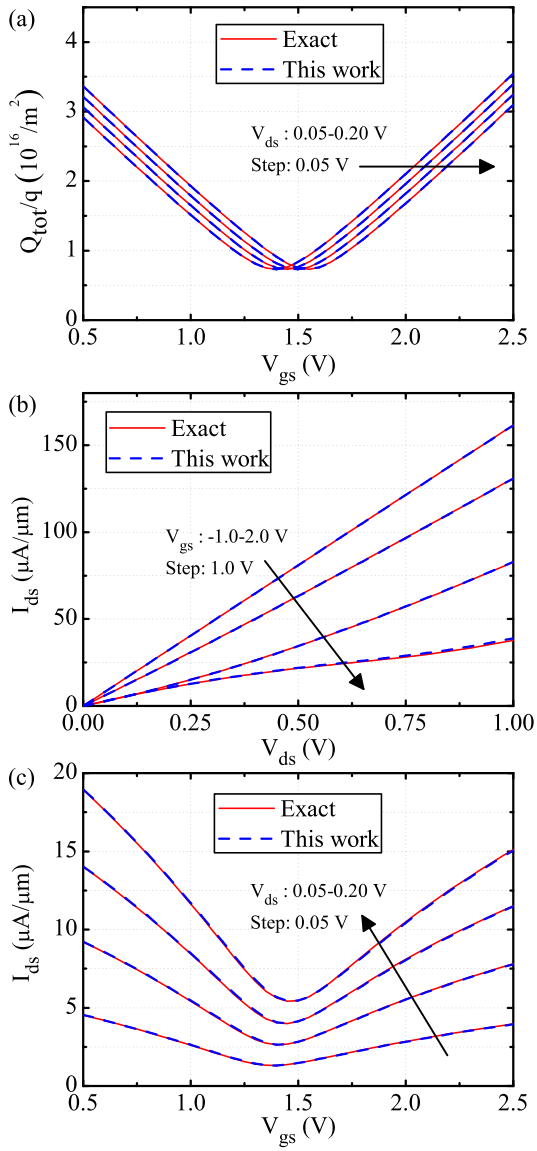

Fig. 6. (a) Charge density on the drain side (Q_{tot}/q versus V_{gs}). (b) Output and (c) transfer characteristics of a 5-μm GFET. The results calculated from the analytical model proposed in this paper is compared with the results achieved from the numerical calculation. The parameters used in the model are $L = 5$ μm, $t_{oxt} = 15$ nm, $k_t = 8.9$, $t_{oxb} = 300$ nm, $k_b = 3.9$, $T = 300$ K, $V_{gs0} = 1.1$ V, $V_{bs0} = 11$ V, $\mu_n = 920$ cm^2/Vs, $\mu_p = 1330$ cm^2/Vs, $\Delta = 92$ meV, $R_{d/s} = 0\ \Omega \cdot \mu$m, and $m = 0.1$ V^2.

A. Numerical Versus Analytical Results

The exact GFET model is calculated numerically using the exact model of parameters, such as α [see (13)], C_q [see (6)], and μ'_{eff} in both electrostatics and electronic transport calculation. Since the elementary mathematical approximation of the first-order Fermi–Dirac integral has a maximum relative error as small as 1.79×10^{-6}, it is used as the exact model in the numerical calculations. In Fig. 6(a), the exact charge density (at the drain side) against V_{gs} under various V_{ds} is compared with the results from the proposed

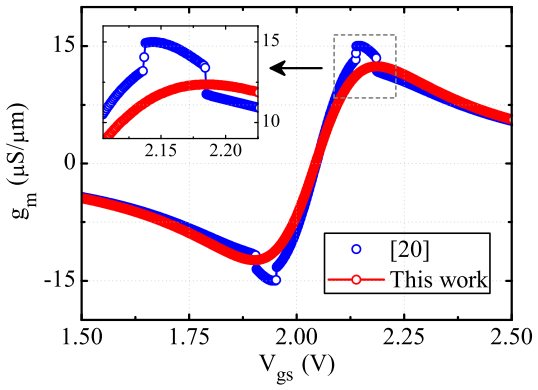

Fig. 7. Comparison of the modeled transconductance g_m versus top-gate to source voltage V_{gs} of a 5-μm GFET [34] in this paper and a model with two-region saturation velocity [20]. Parameters used in the model are taken from [20] except the carrier mobility, and they are $L = 5$ μm, $t_{oxt} = 15$ nm, $k_t = 8.9$, $t_{oxb} = 300$ nm, $k_b = 3.9$, $T = 300$ K, $V_{gs0} = 1.24$ V, $V_{bs0} = 11$ V, $\Delta = 100$ meV, and $R_{d/s} = 3.5$ k$\Omega \cdot \mu$m ($m = 10$ V^2 for this paper and $\hbar\Omega = 75$mV for [20]). $\mu_n = \mu_p = 115\,000$ cm^2/Vs is used here instead of the original 1150 cm^2/Vs to magnify the discontinuity of g_m.

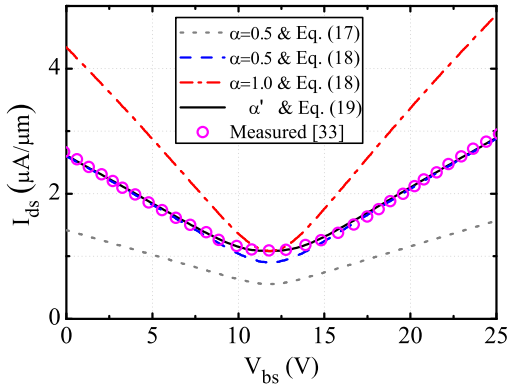

Fig. 8. Comparison of the modeled drain to source current I_{ds} versus back-gate to source voltage V_{bs} of a 2.8-μm GFET [33] in this paper and models using constant α. The parameters used in the models are $L = 2.8$ μm, $t_{oxb} = 285$ nm, $k_b = 3.9$, $T = 300$ K, $V_{bs0} = 11.86$ V, $\mu_n = 430$ cm^2/Vs, $\mu_p = 410$ cm^2/Vs, $\Delta = 64$ meV, $R_{d/s} = 100$ $\Omega \cdot \mu$m, and $m = 0.5$ V^2.

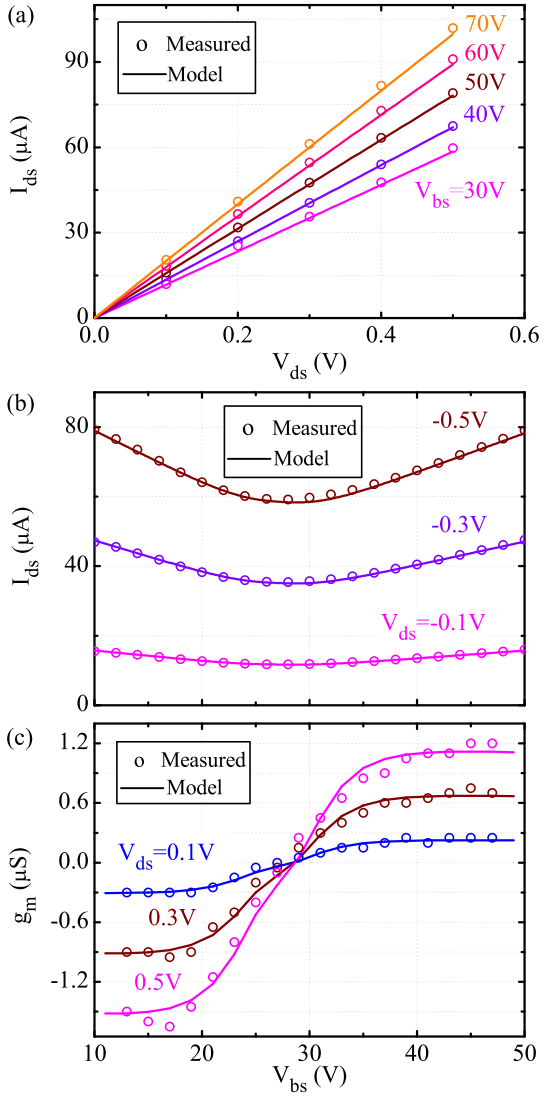

Fig. 9. Modeled output and transfer characteristics of a 20-μm $\times$ 15-μm GFET versus measurement. (a) Drain-to-source current I_{ds} against drain-to-source voltage V_{ds} for various back-gate to source voltage V_{bs}. (b) Drain-to-source current I_{ds} against back-gate-to-source voltage V_{bs} for various drain to source voltages V_{ds}. (c) Transconductance g_m against back-gate-to-source voltage V_{bs} for various drain-to-source voltages V_{ds}. The parameters used in the model are $L = 20$ μm, $W = 15$ μm, $t_{oxb} = 500$ nm, $k_b = 3$, $T = 300$ K, $V_{bs0} = 27.1$ V, $\mu_n = 690$ cm^2/Vs, $\mu_p = 940$ cm^2/Vs, $\Delta = 123$ meV, $R_{d/s} = 3.75$ k$\Omega \cdot \mu$m, and $m = 1$ V^2.

analytical model for a 5-μm GFET. The curves well overlap with each other, and the maximum relative error is only 6.77×10^{-4}. In addition, the comparisons of output and transfer characteristics illustrated in Fig. 6(b) and (c) also show excellent agreement between the exact and analytical results. The maximum relative error in the calculated I_{ds} of this GFET is only 2.89%.

B. Comparison of Models

The two-region model does give a good description of saturation velocity at $q \times |V_{ch}| \ll kT$. However, it results in discontinuous transconductance in the simulation especially when the carrier mobility is high, and thus is ill suited to model GFETs. Fig. 7 shows the comparison between the simulated g_m from the model introduced in [20] and the model developed in this paper for a 5-μm GFET measured by [34]. A high carrier mobility (identical for hole and electron) of 115 000 cm^2/Vs is used instead of 1150 cm^2/Vs (original) to magnify the discontinuities in g_m. It can be seen that discrepancies appear near the maximum and minimum points of g_m and have been corrected by the proposed model thanks to the improved V_{sat} function [see (11)].

In Fig. 8, the simulation results of models using different α and (dV/dV_{ch}) functions are also compared with each other. One can see that the simulation results from the model proposed in this paper agree strongly with the measured data from [33]. The model using $\alpha = 0.5$ and (18) (blue dashed line) differs from the measurement of [33] near the Dirac point and overlaps with the proposed model at high V_{ch}. The underestimation (overestimation) caused using (17) ($\alpha = 1$) is shown by gray dotted line (red dashed-dotted line).

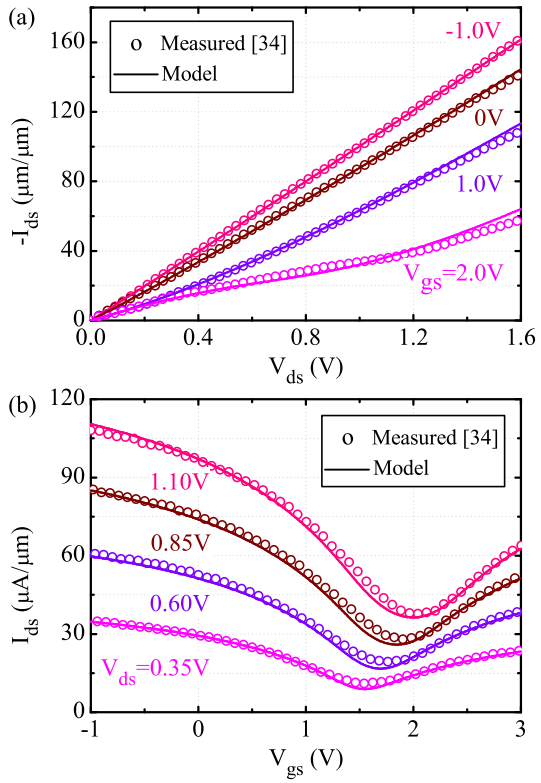

Fig. 10. Modeled transfer characteristics of a 5-μm GFET versus measurement data from [34]. Drain-to-source current $I_{\rm ds}$ against top-gate-to-source voltages $V_{\rm gs}$ for various drain-to-source voltage $V_{\rm ds}$. The parameters used in the model are $L = 5$ μm, $t_{\rm oxt} = 15$ nm, $k_t = 8.9$, $t_{\rm oxb} = 300$ nm, $k_b = 3.9$, $T = 300$ K, $V_{\rm gs0} = 1.1$ V, $V_{\rm bs0} = 11$ V, $\mu_n = 920$ cm^2/Vs, $\mu_p = 1330$ cm^2/Vs, $\Delta = 92$ meV, $R_{d/s} = 2$ k$\Omega \cdot \mu$m, and $m = 0.1$ V^2.

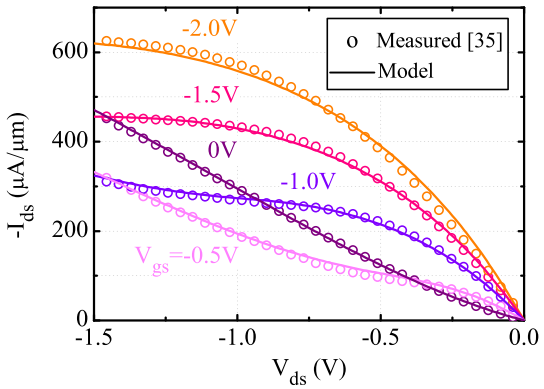

Fig. 11. Modeled output characteristics of a 3-μm GFET against measurement data from [35]. Drain-to-source current $I_{\rm ds}$ against drain-to-source voltage $V_{\rm ds}$ for various gate-to-source voltages $V_{\rm gs}$. The parameters used in the model are $L = 3$ μm, $t_{\rm oxb} = 8.5$ nm, $k_b = 3.5$, $T = 300$ K, $V_{\rm bs0} = -0.07$ V, $\mu_n = 6500$ cm^2/Vs, $\mu_p = 7700$ cm^2/Vs, $\Delta = 66$ meV, $R_{d/s} = 120$ $\Omega \cdot \mu$m, and $m = 0.5$ V^2.

C. Model Versus Measurements

In order to validate the model presented in this paper, a 20-μm $\times$ 15-μm back-gate GFET is fabricated and measured for comparison. The graphene used is CVD graphene transferred onto highly doped Si–SiO_2 wafer with the 80-nm thick Au contacts. The device was annealed for 12 h at 380 K in low vacuum, and the measurement was carried out when the device returned to room temperature. During the fitting procedure, the modeling parameters, such as mobilities, $n_{\rm pud}$, and $R_{d/s}$, are directly fitted on the measured $I_{\rm ds}$. Fig. 9(a)–(c) shows good agreement between the modeled results and the measurements. In addition, the proposed model also achieves good matching with measurement data from [34] and [35] (see Figs. 10 and 11). It can also be seen from Fig. 10 that the transfer characteristics of GFET are accurately modeled for both the electron and hole conduction thanks to the improved carrier mobility analysis of this work. The fitting parameters used in Figs. 8, 10, and 11 are on the same level as those given in [20], [34], and [35].

V. Conclusion

In summary, this paper presents a new concept of effective carrier mobility for GFET modeling. To the best of our knowledge, this is the first time that both the electron and hole mobility difference and the carrier-density-dependent mobility are included in a GFET model. The accurate approximation for saturation velocity proposed in this paper successfully eliminates the discontinuities in the simulated transconductance of GFET models using the two-region $V_{\rm sat}$. The approximation for capacitance weighting factor α proposed in this paper, allowing the transition from $\alpha = 1$ (when $q \times |V_{\rm ch}| \gg kT$) to $\alpha = 0.5$ (when $q \times |V_{\rm ch}| \ll kT$), guarantees the accuracy of the proposed model near the Dirac point and enables closed-form analytical solutions for the drain current. The Verilog-A code of the proposed model supports SPICE-like simulations in commercial simulators. The model has been validated against measurements, and excellent agreement has been achieved for both the electron and hole conduction simultaneously.

References

[1] C.-H. Liu, Y.-C. Chang, T. B. Norris, and Z. Zhong, "Graphene photodetectors with ultra-broadband and high responsivity at room temperature," *Nature Nanotechnol.*, vol. 9, no. 4, pp. 273–278, Mar. 2014.

[2] B. Sensale-Rodriguez *et al.*, "Broadband graphene terahertz modulators enabled by intraband transitions," *Nature Commun.*, vol. 3, Jan. 2012, Art. ID 780.

[3] B. Wu *et al.*, "Experimental demonstration of a transparent graphene millimetre wave absorber with 28% fractional bandwidth at 140 GHz," *Sci. Rep.*, vol. 4, Jan. 2014, Art. ID 4130.

[4] M. C. Lemme, T. J. Echtermeyer, M. Baus, and H. Kurz, "A graphene field-effect device," *IEEE Electron Device Lett.*, vol. 28, no. 4, pp. 282–284, Apr. 2007.

[5] R. Cheng *et al.*, "High-frequency self-aligned graphene transistors with transferred gate stacks," *Proc. Nat. Acad. Sci. USA*, vol. 109, no. 29, pp. 11588–11592, Jul. 2012.

[6] H. Wang, A. Hsu, J. Wu, J. Kong, and T. Palacios, "Graphene-based ambipolar RF mixers," *IEEE Electron Device Lett.*, vol. 31, no. 9, pp. 906–908, Sep. 2010.

[7] H. Wang, D. Nezich, J. Kong, and T. Palacios, "Graphene frequency multipliers," *IEEE Electron Device Lett.*, vol. 30, no. 5, pp. 547–549, May 2009.

[8] L. Vicarelli *et al.*, "Graphene field-effect transistors as room-temperature terahertz detectors," *Nature Mater.*, vol. 11, no. 10, pp. 865–871, Sep. 2012.

[9] M. Foxe *et al.*, "Graphene field-effect transistors on undoped semiconductor substrates for radiation detection," *IEEE Trans. Nanotechnol.*, vol. 11, no. 3, pp. 581–587, May 2012.

[10] I. Meric, M. Y. Han, A. F. Young, B. Ozyilmaz, P. Kim, and K. L. Shepard, "Current saturation in zero-bandgap, top-gated graphene field-effect transistors," *Nature Nanotechnol.*, vol. 3, no. 11, pp. 654–659, Sep. 2008.

[11] S. A. Thiele, J. A. Schaefer, and F. Schwierz, "Modeling of graphene metal-oxide-semiconductor field-effect transistors with gapless large-area graphene channels," *J. Appl. Phys.*, vol. 107, no. 9, p. 094505, 2010.
[12] S. A. Thiele and F. Schwierz, "Modeling of the steady state characteristics of large-area graphene field-effect transistors," *J. Appl. Phys.*, vol. 110, no. 3, p. 034506, 2011.
[13] B. W. Scott and J.-P. Leburton, "Modeling of the output and transfer characteristics of graphene field-effect transistors," *IEEE Trans. Nanotechnol.*, vol. 10, no. 5, pp. 1113–1119, Sep. 2011.
[14] D. Jiménez, "Explicit drain current, charge and capacitance model of graphene field-effect transistors," *IEEE Trans. Electron Devices*, vol. 58, no. 12, pp. 4377–4383, Dec. 2011.
[15] D. Jiménez and O. Moldovan, "Explicit drain-current model of graphene field-effect transistors targeting analog and radio-frequency applications," *IEEE Trans. Electron Devices*, vol. 58, no. 11, pp. 4049–4052, Nov. 2011.
[16] S. Frégonèse *et al.*, "Electrical compact modelling of graphene transistors," *Solid-State Electron.*, vol. 73, pp. 27–31, Jul. 2012.
[17] K. N. Parrish, M. E. Ramón, S. K. Banerjee, and D. Akinwande, "A compact model for graphene FETs for linear and non-linear circuits," in *Proc. IEEE Int. Conf. Simulation Semiconductor Processes Devices (SISPAD)*, Sep. 2012, pp. 75–78.
[18] S. Fregonese, M. Magallo, C. Maneux, H. Happy, and T. Zimmer, "Scalable electrical compact modeling for graphene FET transistors," *IEEE Trans. Nanotechnol.*, vol. 12, no. 4, pp. 539–546, Jul. 2013.
[19] S. Rodriguez *et al.*, "A comprehensive graphene FET model for circuit design," *IEEE Trans. Electron Devices*, vol. 61, no. 4, pp. 1199–1206, Apr. 2014.
[20] G. M. Landauer, D. Jimenez, and J. L. Gonzalez, "An accurate and Verilog-A compatible compact model for graphene field-effect transistors," *IEEE Trans. Nanotechnol.*, vol. 13, no. 5, pp. 895–904, Sep. 2014.
[21] W. Zhu, V. Perebeinos, M. Freitag, and P. Avouris, "Carrier scattering, mobilities, and electrostatic potential in monolayer, bilayer, and trilayer graphene," *Phys. Rev. B*, vol. 80, no. 23, p. 235402, Dec. 2009.
[22] S. Wang, P. K. Ang, Z. Wang, A. L. L. Tang, J. T. L. Thong, and K. P. Loh, "High mobility, printable, and solution-processed graphene electronics," *Nano Lett.*, vol. 10, no. 1, pp. 92–98, Dec. 2009.
[23] V. E. Dorgan, M.-H. Bae, and E. Pop, "Mobility and saturation velocity in graphene on SiO_2," *Appl. Phys. Lett.*, vol. 97, no. 8, p. 082112, 2010.
[24] O. Habibpour, J. Vukusic, and J. Stake, "A large-signal graphene FET model," *IEEE Trans. Electron Devices*, vol. 59, no. 4, pp. 968–975, Apr. 2012.
[25] I. J. Umoh, T. J. Kazmierski, and B. M. Al-Hashimi, "A dual-gate graphene FET model for circuit simulation—SPICE implementation," *IEEE Trans. Nanotechnol.*, vol. 12, no. 3, pp. 427–435, May 2013.
[26] C. Mukherjee, J.-D. Aguirre-Morales, S. Fregonese, T. Zimmer, and C. Maneux, "Versatile compact model for graphene FET targeting reliability-aware circuit design," *IEEE Trans. Electron Devices*, vol. 62, no. 3, pp. 757–763, Mar. 2015.
[27] T. Fang, A. Konar, H. Xing, and D. Jena, "Carrier statistics and quantum capacitance of graphene sheets and ribbons," *Appl. Phys. Lett.*, vol. 91, no. 9, p. 092109, 2007.
[28] J. Deng and H.-S. P. Wong, "A compact SPICE model for carbon-nanotube field-effect transistors including nonidealities and its application—Part II: Full device model and circuit performance benchmarking," *IEEE Trans. Electron Devices*, vol. 54, no. 12, pp. 3195–3205, Dec. 2007.
[29] P. Van Halen and D. L. Pulfrey, "Accurate, short series approximations to Fermi–Dirac integrals of order $-1/2$, $1/2$, 1, $3/2$, 2, $5/2$, 3, and $7/2$," *J. Appl. Phys.*, vol. 57, no. 12, p. 5271, Jun. 1985.
[30] P. Van Halen and D. L. Pulfrey, "Erratum: 'Accurate, short series approximation to Fermi–Dirac integrals of order $-1/2$, $1/2$, 1, $3/2$, 2, $5/2$, 3, and $7/2$' [J. Appl. Phys. 5 7, 5271 (1985)]," *J. Appl. Phys.*, vol. 59, no. 6, p. 2264, Mar. 1986.
[31] *Mathematica Wolfram, Version 9.0.1.0*. [Online]. Available: http://www.wolfram.com/mathematica/, accessed Apr. 24, 2015.
[32] Keysight. *Advanced Design System, Version 2013.06*. [Online]. Available: http://www.keysight.com/en/pc-1297113/advanced-design-system-ads?cc=US%lc=eng, accessed Apr. 24, 2015.
[33] Z. Chen and J. Appenzeller, "Mobility extraction and quantum capacitance impact in high performance graphene field-effect transistor devices," in *Proc. IEEE Int. Electron Devices Meeting*, Dec. 2008, pp. 1–4.
[34] H. Wang, A. Hsu, D. A. Antoniadis, and T. Palacios, "Compact virtual-source current–voltage model for top- and back-gated graphene field-effect transistors," *IEEE Trans. Electron Devices*, vol. 58, no. 5, pp. 1523–1533, May 2011.
[35] I. Meric, C. Dean, A. Young, J. Hone, P. Kim, and K. L. Shepard, "Graphene field-effect transistors based on boron nitride gate dielectrics," in *Proc. IEEE Electron Devices Meeting*, Dec. 2010, pp. 23.2.1–23.2.4.

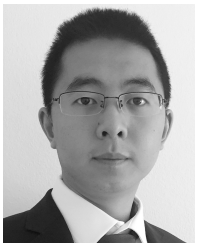

Jing Tian received the B.Sc. degree in solid-state electronics from the University of Electronic Science and Technology of China, Chengdu, China, in 2010, and the M.Sc. degree in electronic engineering from the Tampere University of Technology, Tampere, Finland, in 2013. He is currently pursuing the Ph.D. degree in electronic engineering from the Queen Mary University of London, London, U.K.

Anestis Katsounaros received the Ph.D. degree in antennas and electromagnetics from the Queen Mary University of London, London, U.K., in 2011.

He was a Research Associate of the Antennas and Electromagnetics Group. He is currently a Research Associate with the Cambridge Graphene Center, Cambridge, U.K., and a Visiting Researcher with the Queen Mary University of London, where he is also focusing on high-frequency electronics.

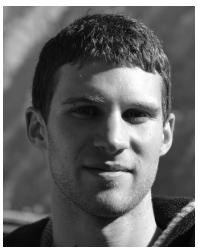

Darryl Smith was born in Maldon, U.K., in 1988. He received the B.Sc. (Hons.) degree in physics with a minor in particle physics and cosmology and the M.Sc. degree in nanoscience to nanotechnology from Swansea University, Swansea, U.K., in 2010 and 2013, respectively. He is currently pursuing the Ph.D. degree in electronic engineering from the Queen Mary University of London, London, U.K.

Yang Hao (F'13) received the Ph.D. degree in computational electromagnetics from the University of Bristol, Bristol, U.K., in 1998.

He is currently a Professor with the Antennas and Electromagnetics Research Group, Queen Mary University of London, London, U.K. His current research interests include graphene and nanomicrowaves, antennas and radio propagation for body centric wireless networks, photonic integrated antennas and computational electromagnetics.